

000 054  
 001 055  
 002 056  
 003 057  
 004 058  
 005 059  
 006 060  
 007 061  
 008 062  
 009 063  
 010 064  
 011 065  
 012 066  
 013 067  
 014 068  
 015 069  
 016 070  
 017 071  
 018 072  
 019 073  
 020 074  
 021 075  
 022 076  
 023 077  
 024 078  
 025 079  
 026 080  
 027 081  
 028 082  
 029 083  
 030 084  
 031 085  
 032 086  
 033 087  
 034 088  
 035 089  
 036 090  
 037 091  
 038 092  
 039 093  
 040 094  
 041 095  
 042 096  
 043 097  
 044 098  
 045 099  
 046 100  
 047 101  
 048 102  
 049 103  
 050 104  
 051 105  
 052 106  
 053 107

## Supplementary File to “Multi-channel Weighted Nuclear Norm Minimization for Real Color Image Denoising”

Anonymous ICCV submission

Paper ID 572

In this supplementary file, we provide:

1. The proof of the Theorem 1 in the main paper.
2. More denoising results on the 24 high quality images from the Kodak PhotoCD dataset.
3. More visual comparisons of denoised images by different methods on the real noisy images of the dataset [1].
4. More visual comparisons of denoised images by different methods on the real noisy images of the dataset [2].

### 1. Proof of Theorem 1.

**Theorem 1.** Assume that the weights in  $w$  are in a non-descending order, the sequence  $\{\mathbf{X}_k\}$ ,  $\{\mathbf{Z}_k\}$ , and  $\{\mathbf{A}_k\}$  generated in Algorithm 1 satisfy:

$$(a) \lim_{k \rightarrow \infty} \|\mathbf{X}_{k+1} - \mathbf{Z}_{k+1}\|_F = 0; \quad (b) \lim_{k \rightarrow \infty} \|\mathbf{X}_{k+1} - \mathbf{X}_k\|_F = 0; \quad (c) \lim_{k \rightarrow \infty} \|\mathbf{Z}_{k+1} - \mathbf{Z}_k\|_F = 0. \quad (1)$$

*Proof.* 1. Firstly, we prove that the sequence  $\{\mathbf{A}_k\}$  generated by Algorithm 1 is upper bounded. Let  $\mathbf{X}_{k+1} + \rho_k^{-1} \mathbf{A}_k = \mathbf{U}_k \Sigma_k \mathbf{V}_k^\top$  be its singular value decomposition (SVD) [3] in the  $(k+1)$ -th iteration. According to Corollary 1 of [4], we can have the SVD of  $\mathbf{Z}_{k+1}$  as  $\mathbf{Z}_{k+1} = \mathbf{U}_k \hat{\Sigma}_k \mathbf{V}_k^\top = \mathbf{U}_k \mathcal{S}_{\frac{w}{\rho_k}}(\Sigma_k) \mathbf{V}_k^\top$ . Then we have

$$\|\mathbf{A}_{k+1}\|_F = \|\mathbf{A}_k + \rho_k (\mathbf{X}_{k+1} - \mathbf{Z}_{k+1})\|_F = \rho_k \|\rho_k^{-1} \mathbf{A}_k + \mathbf{X}_{k+1} - \mathbf{Z}_{k+1}\|_F \quad (2)$$

$$= \rho_k \|\mathbf{U}_k \Sigma_k \mathbf{V}_k^\top - \mathbf{U}_k \mathcal{S}_{\frac{w}{\rho_k}}(\Sigma_k) \mathbf{V}_k^\top\|_F = \rho_k \|\Sigma_k - \mathcal{S}_{\frac{w}{\rho_k}}(\Sigma_k)\|_F \quad (3)$$

$$= \rho_k \sqrt{\sum_i (\Sigma_k^{ii} - \mathcal{S}_{\frac{w}{\rho_k}}(\Sigma_k^{ii}))^2} \leq \rho_k \sqrt{\sum_i \left(\frac{w_i}{\rho_k}\right)^2} = \sqrt{\sum_i w_i^2}. \quad (4)$$

The inequality in the second last step can be proved as follows: given the diagonal matrix  $\Sigma_k$ , we define  $\Sigma_k^{ii}$  as the  $i$ -th element of  $\Sigma_k^{ii}$ . If  $\Sigma_k^{ii} \geq \frac{w_i}{\rho_k}$ , we have  $\mathcal{S}_{\frac{w}{\rho_k}}(\Sigma_k^{ii}) = \Sigma_k^{ii} - \frac{w_i}{\rho_k} \geq 0$ . If  $\Sigma_k^{ii} < \frac{w_i}{\rho_k}$ , we have  $\mathcal{S}_{\frac{w}{\rho_k}}(\Sigma_k^{ii}) = 0 < \Sigma_k^{ii} + \frac{w_i}{\rho_k}$ . After all, we have  $|\Sigma_k^{ii} - \mathcal{S}_{\frac{w}{\rho_k}}(\Sigma_k^{ii})| \leq \frac{w_i}{\rho_k}$  and hence the inequality holds true. Hence, the sequence  $\{\mathbf{A}_k\}$  is upper bounded.

2. Secondly, we prove that the sequence of Lagrangian function  $\{\mathcal{L}(\mathbf{X}_{k+1}, \mathbf{Z}_{k+1}, \mathbf{A}_k, \rho_k)\}$  is also upper bounded. Since the global optimal solution of  $\mathbf{X}$  and  $\mathbf{Z}$  in corresponding subproblems, we always have  $\mathcal{L}(\mathbf{X}_{k+1}, \mathbf{Z}_{k+1}, \mathbf{A}_k, \rho_k) \leq \mathcal{L}(\mathbf{X}_k, \mathbf{Z}_k, \mathbf{A}_k, \rho_k)$ . Based on the updating rule that  $\mathbf{A}_{k+1} = \mathbf{A}_k + \rho_k (\mathbf{X}_{k+1} - \mathbf{Z}_{k+1})$ , we have  $\mathcal{L}(\mathbf{X}_{k+1}, \mathbf{Z}_{k+1}, \mathbf{A}_{k+1}, \rho_{k+1}) = \mathcal{L}(\mathbf{X}_{k+1}, \mathbf{Z}_{k+1}, \mathbf{A}_k, \rho_k) + \langle \mathbf{A}_{k+1} - \mathbf{A}_k, \mathbf{X}_{k+1} - \mathbf{Z}_{k+1} \rangle + \frac{\rho_{k+1} - \rho_k}{2} \|\mathbf{X}_{k+1} - \mathbf{Z}_{k+1}\|_F^2 = \mathcal{L}(\mathbf{X}_{k+1}, \mathbf{Z}_{k+1}, \mathbf{A}_k, \rho_k) + \frac{\rho_{k+1} + \rho_k}{2\rho_k^2} \|\mathbf{A}_{k+1} - \mathbf{A}_k\|_F^2$ . Since the sequence  $\{\|\mathbf{A}_k\|_F\}$  is upper bounded, the sequence  $\{\|\mathbf{A}_{k+1} - \mathbf{A}_k\|_F\}$  is also upper bounded. Denote by  $a$  the upper bound of  $\{\|\mathbf{A}_{k+1} - \mathbf{A}_k\|_F\}$ , we have  $\mathcal{L}(\mathbf{X}_{k+1}, \mathbf{Z}_{k+1}, \mathbf{A}_{k+1}, \rho_{k+1}) \leq \mathcal{L}(\mathbf{X}_1, \mathbf{Z}_1, \mathbf{A}_0, \rho_0) + a \sum_{k=0}^{\infty} \frac{\rho_{k+1} + \rho_k}{2\rho_k^2} = \mathcal{L}(\mathbf{X}_1, \mathbf{Z}_1, \mathbf{A}_0, \rho_0) + a \sum_{k=0}^{\infty} \frac{\mu+1}{2\mu^k \rho_0} \leq \mathcal{L}(\mathbf{X}_1, \mathbf{Z}_1, \mathbf{A}_0, \rho_0) + \frac{a}{\rho_0} \sum_{k=0}^{\infty} \frac{1}{\mu^{k-1}}$ . The last inequality holds since  $\mu+1 < 2\mu$ . Since  $\sum_{k=0}^{\infty} \frac{1}{\mu^{k-1}} < \infty$ , the sequence of Lagrangian function  $\{\mathcal{L}(\mathbf{X}_{k+1}, \mathbf{Z}_{k+1}, \mathbf{A}_{k+1}, \rho_{k+1})\}$  is upper bound.

3. Thirdly, we prove that the sequences of  $\{\mathbf{X}_k\}$  and  $\{\mathbf{Z}_k\}$  are upper bounded. Since  $\|\mathbf{W}(\mathbf{Y} - \mathbf{X})\|_F^2 + \|\mathbf{Z}\|_{w,*} = \mathcal{L}(\mathbf{X}_k, \mathbf{Z}_k, \mathbf{A}_{k-1}, \rho_{k-1}) - \langle \mathbf{A}_k, \mathbf{X}_k - \mathbf{Z}_k \rangle - \frac{\rho_k}{2} \|\mathbf{X}_k - \mathbf{Z}_k\|_F^2 = \mathcal{L}(\mathbf{X}_k, \mathbf{Z}_k, \mathbf{A}_{k-1}, \rho_{k-1}) + \frac{1}{2\rho_k} (\|\mathbf{A}_{k-1}\|_F^2 - \|\mathbf{A}_k\|_F^2)$ . Thus  $\{\mathbf{W}(\mathbf{Y} - \mathbf{X}_k)\}$  and  $\{\mathbf{Z}_k\}$  are upper bounded, and hence the sequence  $\{\mathbf{X}_k\}$  is bounded by the Cauchy-Schwarz inequality

Table 1. PSNR(dB) results of different denoising methods on 24 natural images.

Image#	$\sigma_r = 5, \sigma_g = 30, \sigma_b = 15$								
	CBM3D	MLP	TNRD	NI	NC	WNNM-1	WNNM-2	WNNM-3	MC-WNNM
1	27.25	28.06	28.62	25.00	29.55	28.16	27.95	28.15	
2	29.70	31.30	32.70	27.80	29.69	32.54	31.60	31.73	
3	30.34	31.98	34.07	28.02	31.93	33.91	33.68	33.52	
4	29.47	31.10	32.56	27.70	32.56	32.68	31.85	31.90	
5	27.31	28.59	29.35	26.14	30.00	28.83	29.00	28.91	
6	28.20	29.10	29.90	26.15	28.81	29.55	29.46	29.62	
7	29.73	31.60	33.46	27.22	31.63	33.09	33.29	32.86	
8	27.47	28.16	28.91	25.34	30.16	29.15	29.24	29.03	
9	30.07	31.63	33.55	27.86	31.54	33.19	33.20	32.95	
10	29.96	31.37	33.20	27.74	33.44	32.98	33.02	32.74	
11	28.73	29.85	30.87	26.98	30.16	30.45	30.14	30.21	
12	30.20	31.50	33.31	27.97	31.69	33.22	32.71	32.65	
13	26.18	26.69	26.98	25.14	27.97	26.49	26.42	26.62	
14	27.86	29.07	29.87	26.67	29.21	29.36	29.14	29.30	
15	29.91	31.58	33.13	28.04	31.17	33.22	32.34	32.36	
16	29.29	30.35	31.54	27.46	32.18	31.34	31.05	31.21	
17	29.50	31.09	32.52	27.81	32.80	32.09	32.00	31.85	
18	27.72	28.74	29.36	26.57	28.63	28.88	28.76	28.89	
19	28.98	30.18	31.35	27.25	29.79	31.34	30.77	30.95	
20	30.63	31.78	33.27	27.89	29.52	33.00	32.55	32.58	
21	28.50	29.58	30.54	26.86	31.71	30.02	30.03	30.03	
22	28.61	29.78	30.82	27.19	30.50	30.47	29.82	30.10	
23	30.60	32.66	35.06	28.17	32.82	34.72	34.37	33.94	
24	27.97	28.81	29.61	26.01	30.75	29.47	29.35	29.39	
Average	28.92	30.19	31.44	27.04	30.76	31.17	30.91	30.89	<b>32.70</b>

and triangle inequality. We can obtain that  $\lim_{k \rightarrow \infty} \|\mathbf{X}_{k+1} - \mathbf{Z}_{k+1}\|_F = \lim_{k \rightarrow \infty} \rho_k^{-1} \|\mathbf{A}_{k+1} - \mathbf{A}_k\|_F = 0$  and the equation (a) is proved.

4. Then we can prove that  $\lim_{k \rightarrow \infty} \|\mathbf{X}_{k+1} - \mathbf{X}_k\|_F = \lim_{k \rightarrow \infty} \|(\mathbf{W}^\top \mathbf{W} + \frac{\rho_k}{2} \mathbf{I})^{-1} (\mathbf{W}^\top \mathbf{W} \mathbf{Y} - \mathbf{W}^\top \mathbf{W} \mathbf{Z}_k - \frac{1}{2} \mathbf{A}_k) - \rho_k^{-1} (\mathbf{A}_k - \mathbf{A}_{k-1})\|_F \leq \lim_{k \rightarrow \infty} \|(\mathbf{W}^\top \mathbf{W} + \frac{\rho_k}{2} \mathbf{I})^{-1} (\mathbf{W}^\top \mathbf{W} \mathbf{Y} - \mathbf{W}^\top \mathbf{W} \mathbf{Z}_k - \frac{1}{2} \mathbf{A}_k)\|_F + \rho_k^{-1} \|\mathbf{A}_k - \mathbf{A}_{k-1}\|_F = 0$  and hence (b) is proved.

5. Finally, (c) can be proved by checking that  $\lim_{k \rightarrow \infty} \|\mathbf{Z}_{k+1} - \mathbf{Z}_k\|_F = \lim_{k \rightarrow \infty} \|\mathbf{X}_k + \rho_k^{-1} \mathbf{A}_{k-1} - \mathbf{Z}_k + \mathbf{X}_{k+1} - \mathbf{X}_k + \rho_k^{-1} \mathbf{A}_{k-1} + \rho_k^{-1} \mathbf{A}_k - \rho_k^{-1} \mathbf{A}_{k+1}\|_F \leq \lim_{k \rightarrow \infty} \|\Sigma_{k-1} - \mathcal{S}_{w/\rho_{k-1}}(\Sigma_{k-1})\|_F + \|\mathbf{X}_{k+1} - \mathbf{X}_k\|_F + \rho_k^{-1} \|\mathbf{A}_{k-1} + \mathbf{A}_{k+1} - \mathbf{A}_k\|_F = 0$ , where  $\mathbf{U}_{k-1} \Sigma_{k-1} \mathbf{V}_{k-1}^\top$  is the SVD of the matrix  $\mathbf{X}_k + \rho_{k-1} \mathbf{A}_{k-1}$ .  $\square$

## 2. More denoising results on the 24 high quality images from the Kodak PhotoCD dataset

In the main paper, we have given the PSNR results of the competing methods on the 24 high quality images from the Kodak PhotoCD dataset when the standard deviations of the additive white Gaussian noise (AWGN) are  $\sigma_r = 40, \sigma_g = 20, \sigma_b = 30$  for R, G, B channels, respectively. Here we provide more denoising results on this dataset. In Tables ??-??, we give more PSNR results on these images when the noise standard deviations are  $\sigma_r = 5, \sigma_g = 30, \sigma_b = 15$  in Table 1 and  $\sigma_r = 30, \sigma_g = 10, \sigma_b = 50$  in Table 2, respectively. In Figures 3-??, we give the visual comparisons of the denoised images by different methods.

Fig. 3 shows a scene denoised by the compared methods. We can see that the methods of CBM3D and NC would remain some noise on the recovered images. The methods of MLP, TNRD, and “WNNM-1”, which process separately the channels of color images, would over-smooth the images and generate false colors or artifacts. The method “WNNM-2”, which process jointly the channels of color images, would not generate false colors, but still over-smooth the image. The “WNNM-3”, which is the WNNM model solved by ADMM algorithm, would remain some noise on the image. By employing the proposed MC-WNNM model, our method preserves the structures (e.g., textures in windows and grass) better across the R, G, B channels and generate less artifacts than other denoising methods, leading to visually pleasant outputs.

Table 2. PSNR(dB) results of different denoising methods on 24 natural images.

Image#	CBM3D	MLP	TNRD	NI	NC	WNNM-1	WNNM-2	WNNM-3	MC-WNNM
1	23.38	26.49	26.50	24.82	23.59	26.40	25.60		
2	25.19	30.94	30.90	26.82	27.79	30.89	29.75		
3	25.39	32.03	32.09	27.52	27.41	32.20	31.17		
4	24.96	30.55	30.47	27.34	27.00	30.74	29.71		
5	23.29	26.65	26.73	25.72	26.67	26.74	25.98		
6	24.09	27.76	27.70	26.10	26.12	27.85	26.96		
7	24.89	30.70	30.72	27.17	28.07	30.91	29.94		
8	23.30	26.12	26.27	25.59	26.11	26.87	26.33		
9	25.20	31.35	31.31	27.74	28.33	31.30	30.45		
10	25.13	31.01	31.05	27.60	28.53	31.12	30.17		
11	24.54	28.79	28.82	26.72	24.40	28.73	27.79		
12	25.43	31.60	31.60	27.82	29.01	31.59	30.62		
13	22.50	24.71	24.73	24.96	23.36	24.70	23.85		
14	23.91	27.69	27.72	26.26	23.08	27.62	26.81		
15	25.45	31.09	31.05	27.36	28.49	31.29	30.21		
16	24.89	29.79	29.73	27.35	27.10	29.84	28.85		
17	25.12	30.26	30.24	27.15	27.54	30.11	29.35		
18	23.83	27.26	27.26	26.05	26.15	27.32	26.18		
19	24.63	29.40	29.39	27.06	27.41	29.78	28.87		
20	26.43	31.16	31.27	26.43	26.92	31.25	30.43		
21	24.24	28.26	28.27	26.66	27.18	28.22	27.45		
22	24.51	29.03	29.06	26.83	27.64	29.02	27.81		
23	25.55	32.87	32.75	27.60	23.75	32.58	31.46		
24	23.85	27.06	27.13	25.86	27.05	27.50	26.63		
<b>Average</b>	24.57	29.27	29.28	26.69	26.61	29.36	28.43		<b>29.90</b>

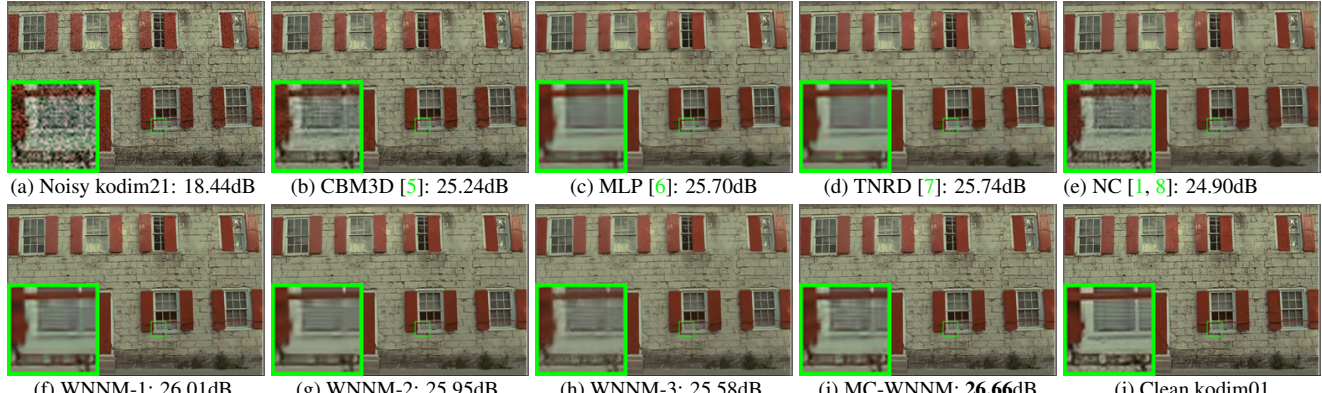


Figure 1. Denoised images of different methods on the image “kodim01” degraded by AWGN with different standard deviations of  $\sigma_r = 40, \sigma_g = 20, \sigma_b = 30$  on R, G, B channels, respectively. The images are better to be zoomed in on screen.

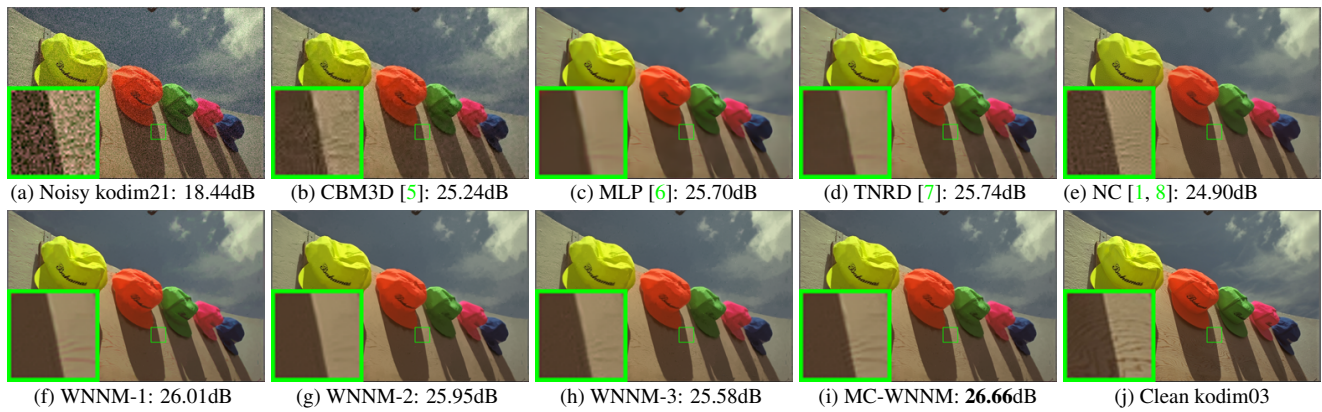


Figure 2. Denoised images of different methods on the image “kodim03” degraded by AWGN with different standard deviations of  $\sigma_r = 40, \sigma_g = 20, \sigma_b = 30$  on R, G, B channels, respectively. The images are better to be zoomed in on screen.

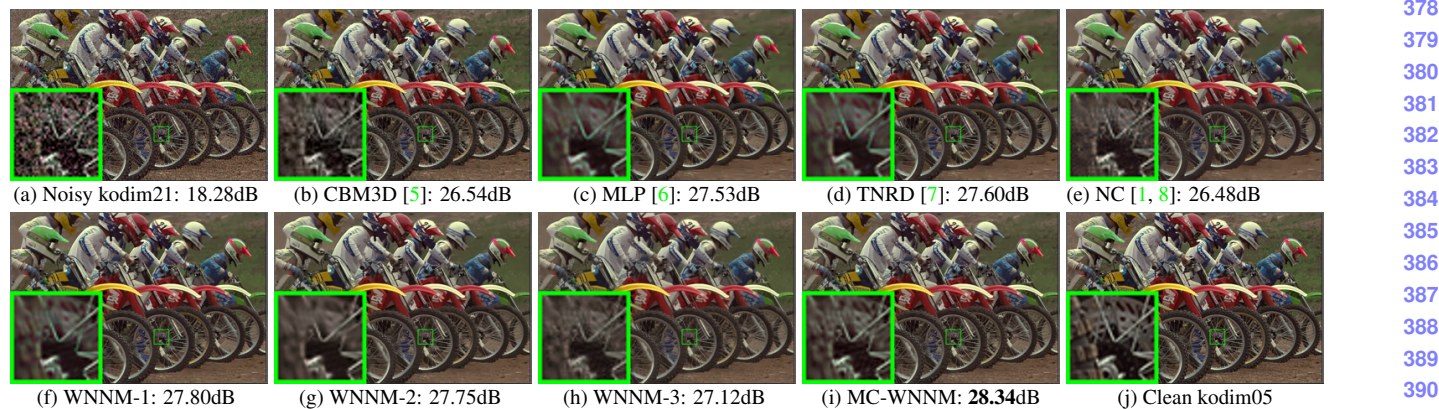


Figure 3. Denoised images of different methods on the image “kodim05” degraded by AWGN with different standard deviations of  $\sigma_r = 40$ ,  $\sigma_g = 20$ ,  $\sigma_b = 30$  on R, G, B channels, respectively. The images are better to be zoomed in on screen.

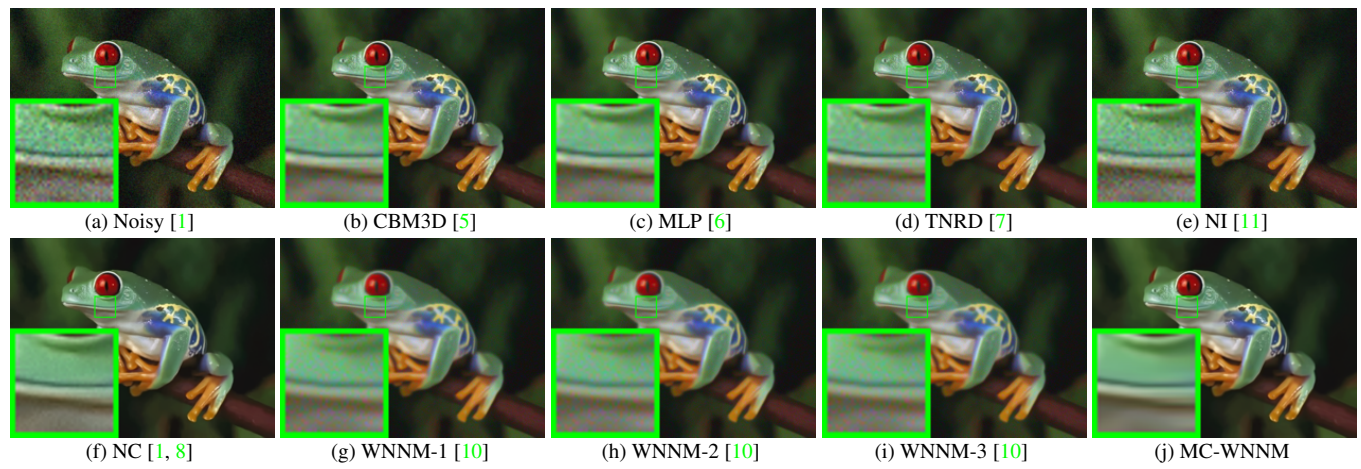


Figure 4. Denoised images of the real noisy image “Frog” [1] by different methods. The images are better to be zoomed in on screen.

### 3. More visual comparisons of denoised images by different methods on the real noisy images of the dataset [1]

In this section, we give more comparisons of the state-of-the-art denoising methods on the dataset [1]. The real noisy images in dataset [1] have no “ground truth” images and hence we only compare the visual quality of the denoised images by different methods. As can be seen from Figures ??-??, our proposed method performs better than the competing methods.

### 4. More visual comparisons of denoised images by different methods on the real noisy images of the dataset [2]

In this section, we provide more comparisons of the proposed method with the state-of-the-art denoising methods on the 15 cropped real noisy images used in [2]. In this dataset, each scene was shot 500 times under the same camera and camera setting. The mean image of the 500 shots is roughly taken as the “ground truth”, with which the PSNR can be computed. As can be seen from Figures 10-??, in most cases, our proposed method achieves better performance than the the competing methods. This validates the effectiveness of our proposed external prior guided internal prior learning framework for real noisy image denoising.

## References

- [1] M. Lebrun, M. Colom, and J. M. Morel. The noise clinic: a blind image denoising algorithm. <http://www.ipol.im/pub/art/2015/125/>. Accessed 01 28, 2015. 1, 3, 4, 5, 6, 7, 8

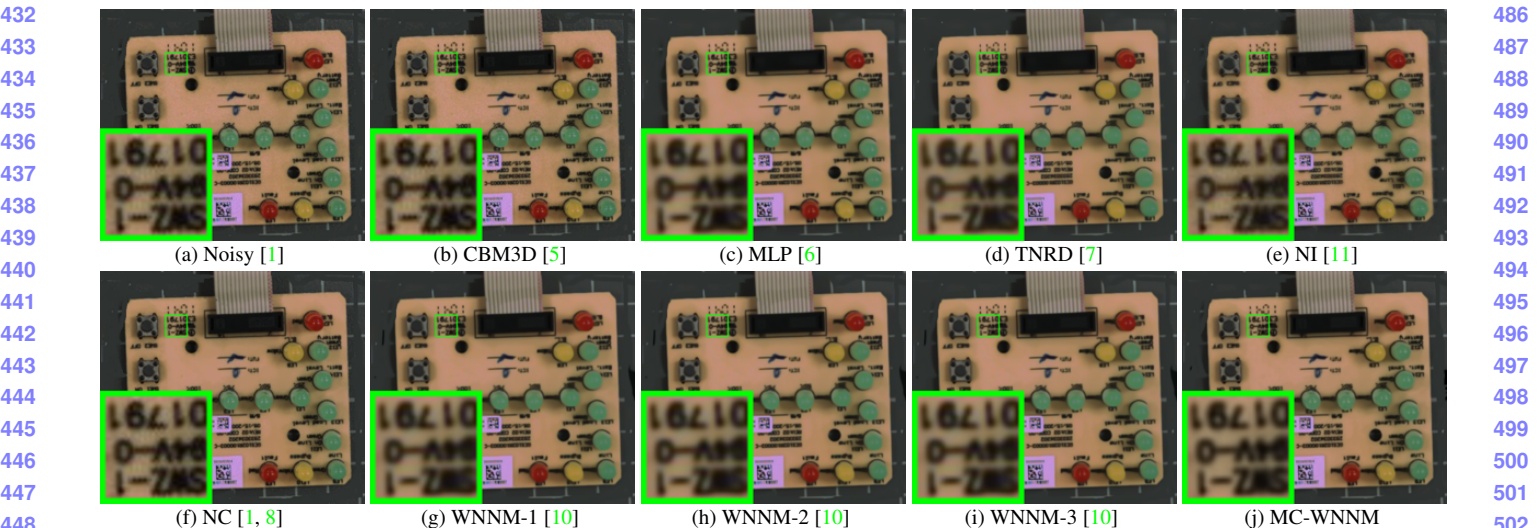


Figure 5. Denoised images of the real noisy image “Circuit” [1] by different methods. The images are better to be zoomed in on screen.

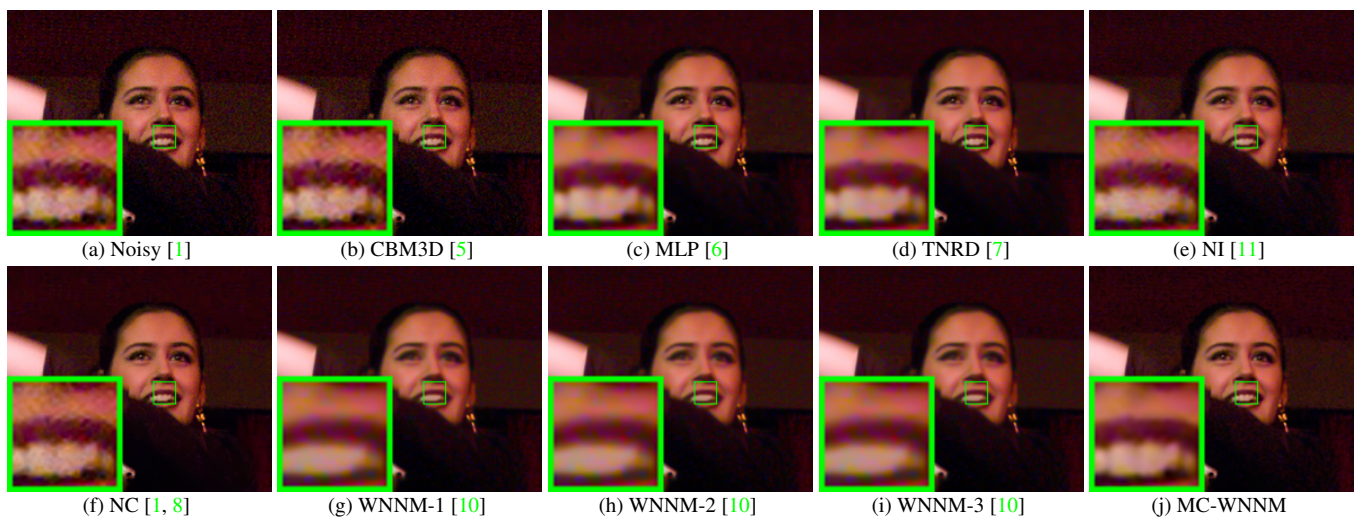


Figure 6. Denoised images of the real noisy image “Woman” [1] by different methods. The images are better to be zoomed in on screen.

- [2] S. Nam, Y. Hwang, Y. Matsushita, and S. J. Kim. A holistic approach to cross-channel image noise modeling and its application to image denoising. *IEEE Conference on Computer Vision and Pattern Recognition (CVPR)*, pages 1683–1691, 2016. 1, 4, 6, 7, 8
- [3] C. Eckart and G. Young. The approximation of one matrix by another of lower rank. *Psychometrika*, 1(3):211–218, 1936. 1
- [4] S. Gu, Q. Xie, D. Meng, W. Zuo, X. Feng, and L. Zhang. Weighted nuclear norm minimization and its applications to low level vision. *International Journal of Computer Vision*, pages 1–26, 2016. 1
- [5] K. Dabov, A. Foi, V. Katkovnik, and K. Egiazarian. Color image denoising via sparse 3D collaborative filtering with grouping constraint in luminance-chrominance space. *IEEE International Conference on Image Processing (ICIP)*, pages 313–316, 2007. 3, 4, 5, 6, 7, 8
- [6] H. C. Burger, C. J. Schuler, and S. Harmeling. Image denoising: Can plain neural networks compete with BM3D? *IEEE Conference on Computer Vision and Pattern Recognition (CVPR)*, pages 2392–2399, 2012. 3, 4, 5, 6, 8
- [7] Y. Chen, W. Yu, and T. Pock. On learning optimized reaction diffusion processes for effective image restoration. *IEEE Conference on Computer Vision and Pattern Recognition (CVPR)*, pages 5261–5269, 2015. 3, 4, 5, 6, 7, 8
- [8] M. Lebrun, M. Colom, and J.-M. Morel. Multiscale image blind denoising. *IEEE Transactions on Image Processing*, 24(10):3149–3161, 2015. 3, 4, 5, 6, 7, 8

486  
487  
488  
489  
490  
491  
492  
493  
494  
495  
496  
497  
498  
499  
500  
501  
502  
503  
504  
505  
506  
507  
508  
509  
510  
511  
512  
513  
514  
515  
516  
517  
518  
519  
520  
521  
522  
523  
524  
525  
526  
527  
528  
529  
530  
531  
532  
533  
534  
535  
536  
537  
538  
539

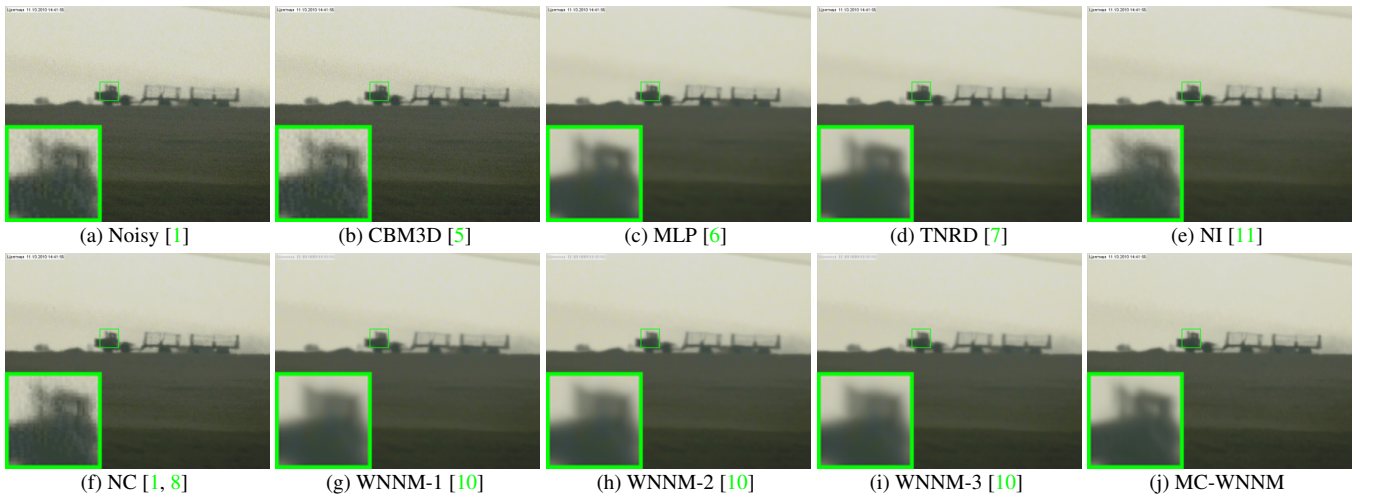


Figure 7. Denoised images of the real noisy image “Vehicle” [1] by different methods. The images are better to be zoomed in on screen.

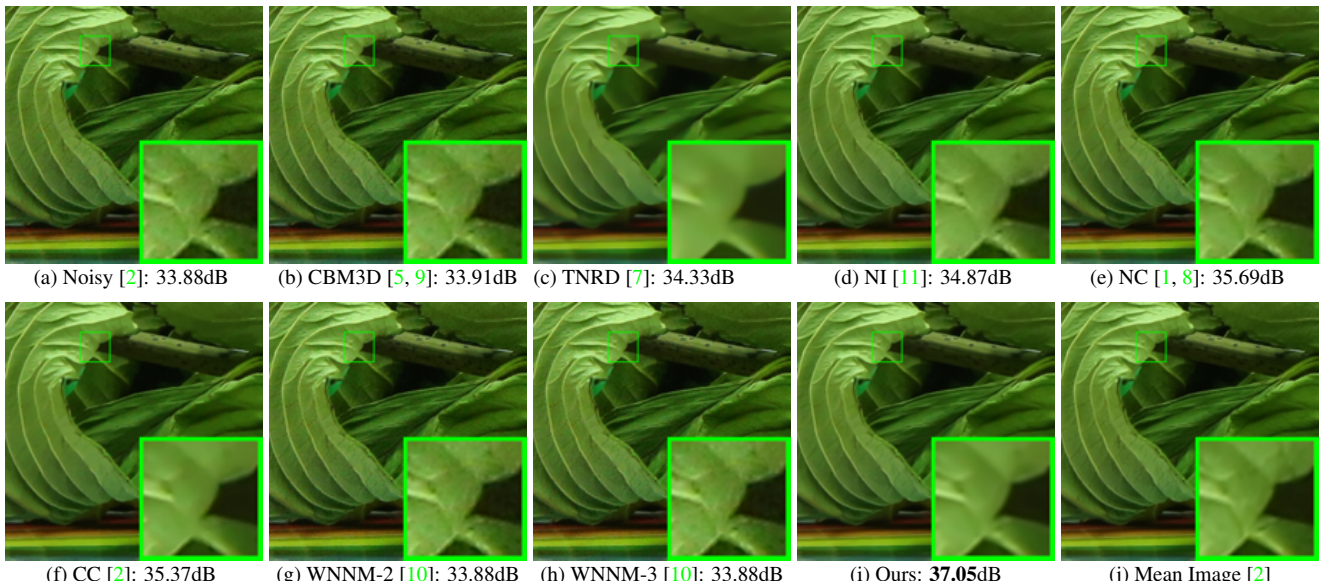


Figure 8. Denoised images of a region cropped from the real noisy image “Canon 5D Mark 3 ISO 3200 2” [2] by different methods. The images are better to be zoomed in on screen.

- [9] K. Dabov, A. Foi, V. Katkovnik, and K. Egiazarian. Image denoising by sparse 3-D transform-domain collaborative filtering. *IEEE Transactions on Image Processing*, 16(8):2080–2095, 2007. 6, 7, 8
- [10] S. Gu, L. Zhang, W. Zuo, and X. Feng. Weighted nuclear norm minimization with application to image denoising. *IEEE Conference on Computer Vision and Pattern Recognition (CVPR)*, pages 2862–2869, 2014. 4, 5, 6, 7, 8
- [11] Neatlab ABSoft. Neat Image. <https://ni.neatvideo.com/home>. 4, 5, 6, 7, 8



756  
757  
758  
759  
760  
761  
762  
763  
764  
765  
766  
767  
768  
769  
770  
771  
772  
773  
774  
775  
776  
777  
778  
779  
780  
781  
782  
783  
784  
785  
786  
787  
788  
789  
790  
791  
792  
793  
794  
795  
796  
797  
798  
799  
800  
801  
802  
803  
804  
805  
806  
807  
808  
809

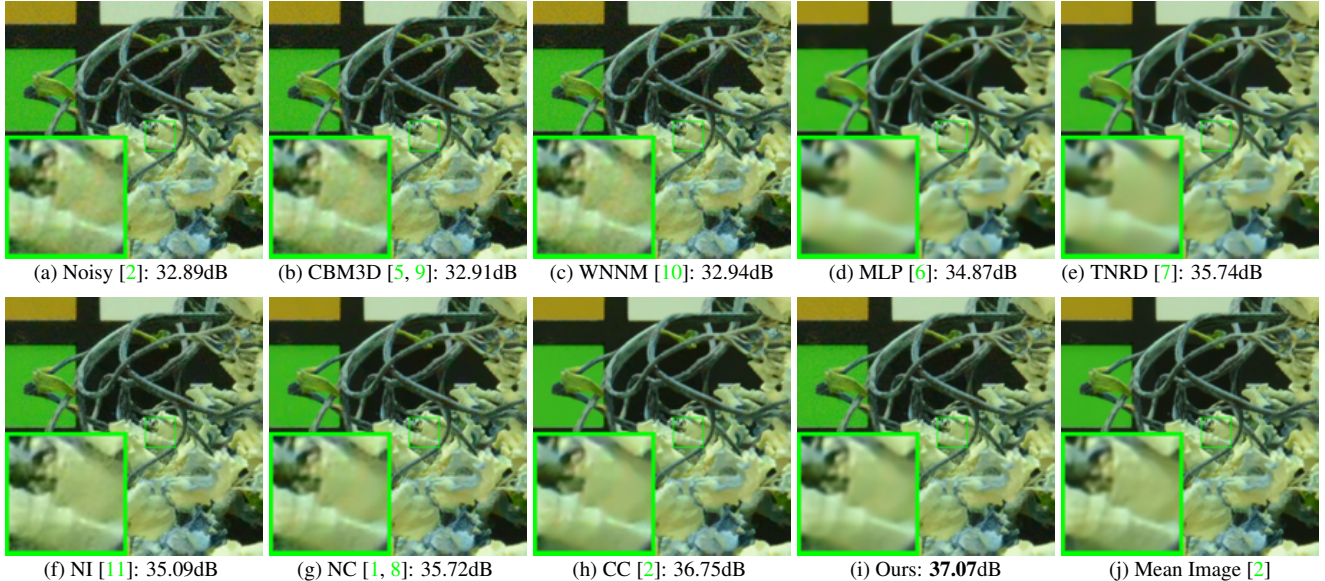


Figure 11. Denoised images of a region cropped from the real noisy image “Nikon D800 ISO 6400 2” [2] by different methods. The images are better to be zoomed in on screen.

810  
811  
812  
813  
814  
815  
816  
817  
818  
819  
820  
821  
822  
823  
824  
825  
826  
827  
828  
829  
830  
831  
832  
833  
834  
835  
836  
837  
838  
839  
840  
841  
842  
843  
844  
845  
846  
847  
848  
849  
850  
851  
852  
853  
854  
855  
856  
857  
858  
859  
860  
861  
862  
863